Article

Not peer-reviewed version

Barbaloin Alleviates Lung Ischemia-Reperfusion Injury by Dual-Targeting IL-6 and PNP

Huanhuan Dong †, Niuniu Dong †, Jinteng Feng †, Wenyu Peng *, Zhiying Wang, Yihan Lin, Zixuan Zhao, Xiaopeng Ma, Rongxuan Jiang, Yanpeng Zhang *, Mao Sun *, Guangjian Zhang *

Posted Date: 8 April 2026

doi: 10.20944/preprints202604.0528.v1

Keywords: lung transplantation; ischemia-reperfusion injury; barbaloin; IL-6; PNP; oxidative stress; NF-κB/NLRP3 inflammasome

 doi:10.20944/preprints202604.0528.v1

Article

Barbaloin Alleviates Lung Ischemia-Reperfusion Injury by Dual-Targeting IL-6 and PNP

Huanhuan Dong [1,2,†], Niuniu Dong [1,†], Jinteng Feng [1,†], Wenyu Peng [3,*], Zhiying Wang [1], Yihan Lin [1], Zixuan Zhao [4], Xiaopeng Ma [1], Rongxuan Jiang [1], Yanpeng Zhang [1,*], Mao Sun [3,*] and Guangjian Zhang [1,*]

[1] Department of Thoracic Surgery, The First Affiliated Hospital of Xi'an Jiaotong University, Xi'an 710032, Shaanxi, China

[2] Center of Precision Medicine Research, The First Affiliated Hospital of Xi'an Jiaotong University, Xi'an 710032, Shaanxi, China

[3] Department of Biochemistry and Molecular Biology, School of Basic Medicine, Fourth Military Medical University, Xi'an 710032, China

[4] Department of Biomedical Engineering, The University of Melbourne, Melbourne 3010, Victoria, Australia

* Correspondence: yuwenpeng@fmmu.edu.cn (W.P.); yanpeng_zhang@xjtu.edu.cn (Y.Z.); sm060075@fmmu.edu.cn (M.S.), michael8039@xjtu.edu.cn (G.Z.)

† Equally contributed to this work.

Abstract

Ischemia-reperfusion injury (IRI) is a primary driver of graft dysfunction following lung transplantation, yet effective therapeutic strategies remain limited. Through integrated multi-omics analysis, target prediction, and experimental validation, this study identifies barbaloin as a potent dual-target agent that alleviates lung IRI by simultaneously inhibiting interleukin-6 (IL-6) and purine nucleoside phosphorylase (PNP). Mechanistically, barbaloin reduces intracellular Reactive Oxygen Species (ROS) accumulation by suppressing both IL-6 and PNP, thereby abrogating the ROS-dependent NF-κB/NLRP3 signaling cascade and subsequent immune-inflammatory responses. These findings highlight the pivotal role of the IL-6/PNP axis in mediating barbaloin's antioxidant and anti-inflammatory effects. Furthermore, barbaloin's favorable ADMET profile supports its potential as a novel therapeutic candidate for lung transplantation and other oxidative stress-driven inflammatory disorders.

Keywords: lung transplantation; Ischemia-reperfusion injury; Barbaloin; IL-6; PNP; oxidative stress; NF-κB/NLRP3 inflammasome

1. Introduction

Ischemia-reperfusion injury (IRI) is characterized by a complex multisystem response to a prolonged interruption in organ perfusion followed by restoration of that perfusion, it is universal in varying organ transplantation, but particularly relevant in the lung transplant population, as transplanted lungs remain the most at-risk clinically of the transplanted solid organ [1]. IRI in the transplanted lung is characterized by sterile inflammation, microvascular permeability, endothelial cell (EC) dysfunction, and pulmonary edema with increased pulmonary vascular resistance and impaired oxygen exchange. It has been described clinically as primary graft dysfunction (PGD) [2]. Lung IRI (LIRI) and the resulting PGD leads to serious adverse outcomes in patients and increases the overall burden of lung transplantation on the healthcare system. Understand the mechanism of LIRI to improve the outcomes of lung transplantation is essential [3]. Several studies have shown that the ischemia accompanied by the release of damage-associated molecules that can bind to their corresponding receptors, leading to the upregulation of cytokine production, with devastating inflammatory reactions upon reperfusion [4]. Although extensive research endeavors have been

 doi:10.20944/preprints202604.0528.v1

undertaken, few preventative and therapeutic treatments have emerged for clinical use. Novel strategies are still needed to improve outcomes after lung transplantation [5].

Barbaloin, the major anthraquinone glycoside isolated from Aloe vera, is traditionally known as a bittering agent [6]. Beyond this, it possesses a broad spectrum of reported pharmacological properties, including anti-inflammatory, anti-apoptotic, anti-tumor, and potent antioxidant activities [7]. Of particular relevance, preclinical studies have demonstrated its protective efficacy in injury models sharing pathophysiological features with LIRI. For instance, barbaloin has been shown to protect against lipopolysaccharide-induced acute lung injury by inhibiting the ROS-mediated PI3K/AKT/NF-κB pathway [8]. Furthermore, in myocardial ischemia-reperfusion models, barbaloin pretreatment attenuates injury by activating AMPK, improving hemodynamics, and limiting infarct size [9].

Given this promising pharmacological profile and its efficacy in related inflammatory and ischemic conditions, we hypothesized that barbaloin may confer protective effects in the specific context of LIRI. In this study, we employed an integrated multi-omics and experimental verification to systematically investigate this hypothesis. Our analyses identified that IL-6 and PNP as central mediators of early post-transplant injury and demonstrated that barbaloin can stably interact with these two targets. Subsequent in vitro experiment confirmed that barbaloin mitigates oxygen-glucose deprivation/reoxygenation (OGD/R) injury in bronchial epithelial cells by reducing oxidative stress and suppressing the NF-κB/NLRP3 inflammasome pathway. Taken together, these findings highlight the therapeutic potential of barbaloin in attenuating inflammation and tissue injury associated with lung transplantation.

2. Results

2.1. Integrated Transcriptomic Analysis of Human Lung Transplant Biopsies

Transcriptomic data from two independent human lung transplantation cohorts (GSE127004, 46 paired samples; GSE145989, 67 paired samples) were integrated for analysis. All samples comprised peripheral lung biopsies collected at the end of cold ischemia (cit) and 1-2 hours post-reperfusion (1-2 hr), resulting in 113 matched pairs after batch effects corrected, data normalized and validation (Supplementary Figure S1). Gene Set Enrichment Analysis (GSEA) of the combined dataset identified the top 10 differentially regulated pathways between cit and 1-2 hr groups (Figure 1A), which mainly segregated into two major functional phenotype, the upregulated pathways of immune-inflammatory activation (including IL-17/TNF/NF-κB signaling, cytokine-cytokine receptor interaction, and lipid and atherosclerosis), and downregulated pathways of metabolic suppression (involving taurine/propanoate/pyruvate metabolism, peroxisome-mediated fatty acid oxidation, and cytochrome P450 metabolism). To identify the key drivers of this phenotype, differential expression analysis yielding 362 significantly altered genes (DEGs; $q < 0.05$, $|\log_2 FC| > 0.585$), with 319 upregulated and 43 downregulated (Figure 1B). A weighted gene co-expression network (WGCNA) was then constructed to define functionally coordinated gene modules. Using a soft-thresholding power of 4 (scale-free topology fit $R^2 \geq 0.85$; Figure 1C，D), six distinct co-expression modules were identified (Figure 1E). The turquoise (204 genes) and yellow (74 genes) modules demonstrated the strongest positive correlation with the transplantation phenotype (Figure 1F). The yellow module was associated with acute innate immune effector functions (e.g., neutrophil activation), while the ME turquoise module was enriched for broad inflammatory signaling pathways (e.g., IL-17, TNF, NF-κB), suggesting a role in sustaining inflammatory responses (Supplementary Figure S2). High correlations between gene significance (GS) and module membership (MM) for both modules (Turquoise: $r = 0.76$, $p = 9e\text{-}44$; Yellow: $r = 0.54$, $p = 2e\text{-}18$; Figure 1G, H) confirmed their biological relevance, which establishing 278 high-confidence candidate genes. To further narrow down the screening range of the key driving gene, the overlap of 175 candidate genes between the 362 DEGs and the 278 WGCNA was identified (Figure 1I). Additionally, a reference set of 4,100 genes associated with “Lung Transplantation” was compiled from the GeneCards and OMIM databases (Figure 1J).

 doi:10.20944/preprints202604.0528.v1

All gene lists are provided in the supplementary tables: DEGs and phenotype-linked WGCNA modules (Supplementary Table S1), and the reference gene set derived from GeneCards and OMIM (Supplementary Table S2).

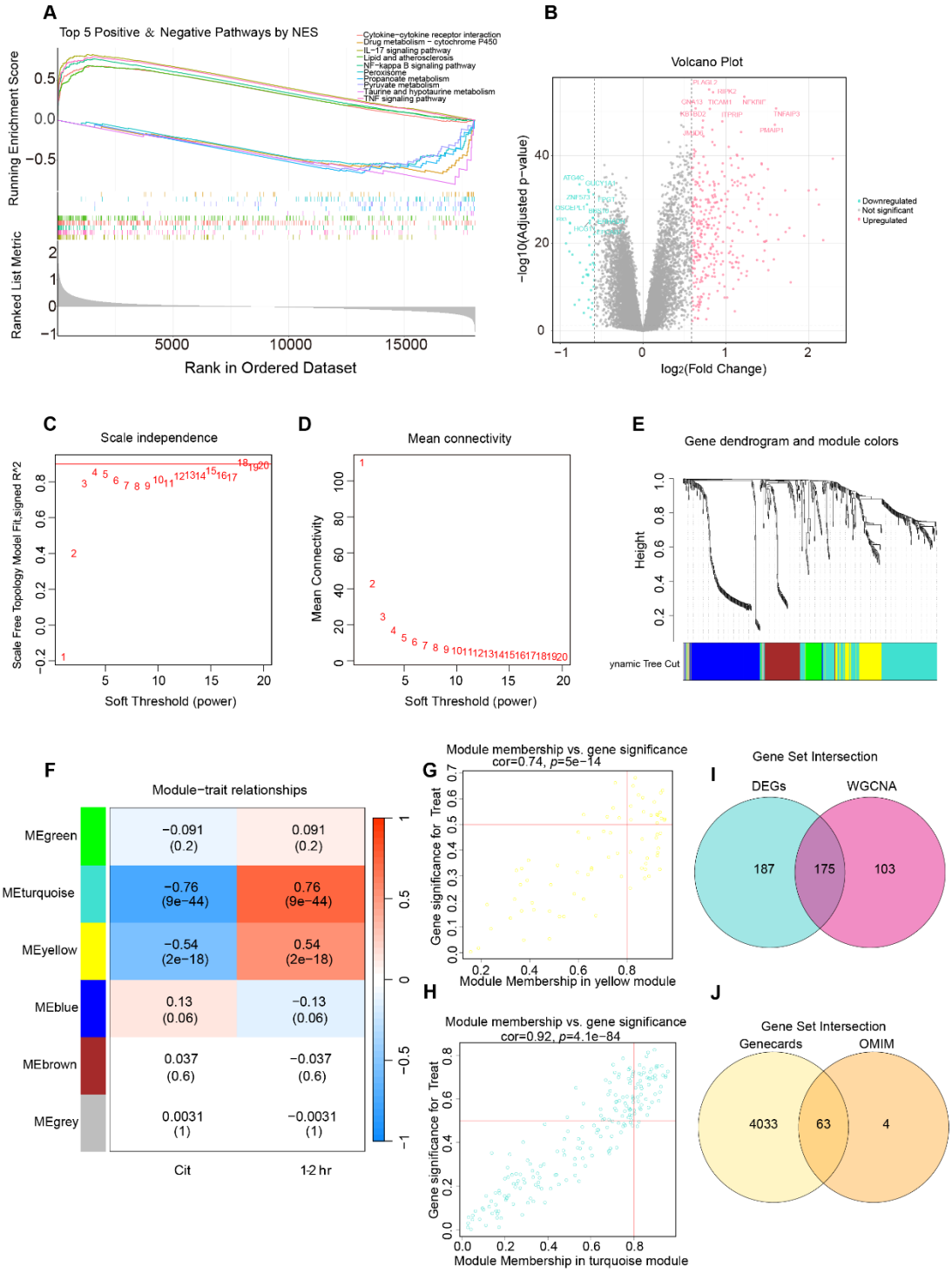

Figure 1. Identification of lung transplantation related candidate genes. A) Gene set enrichment analysis (GSEA) of the merged datasets GSE127003 and GSE145989. B) Volcano plot of differential expression genes. C) Scale free fit analysis for selecting the soft threshold power in weighted gene co expression network analysis (WGCNA). D) Mean connectivity analysis for soft threshold power selection in WGCNA. E) Clustering dendrogram of genes and module identification by WGCNA. F) Module-trait relationship heatmap; two lung transplantation associated modules were identified (Yellow: 74 genes; Turquoise: 204 genes), whose union yielded 278 genes. G,

 doi:10.20944/preprints202604.0528.v1

H) Scatter plots of gene significance (GS) versus module membership (MM) for the yellow (G) and turquoise (H) modules. I) Venn diagram showing the overlap between the 362 DEGs and the 278 WGCNA derived module genes. J) Venn diagram showing the union of lung transplantation related genes retrieved from the GeneCards database (4096 genes, Gifts ≥ 5) and the OMIM database (67 genes), resulting in 4100 candidate genes.

2.2. Barbaloin Structure Acquisition and Target Gene Prediction

The two-dimensional (2D) structure of barbaloin was generated with ChemBio3D (v14.0) and its SMILES notation was obtained for target prediction (Figure 2A). To systematically identify potential molecular targets, in silico screening was performed using four independent platforms: PharmMapper, the Similarity Ensemble Approach (SEA), SuperPred, and SwissTargetPrediction (Figure 2B). Initial predictions yielded 290, 32, 104, and 102 targets from each platform, respectively. After merging and deduplication, a final set of 455 unique genes was compiled as the predicted target pool for barbaloin (Supplementary Table S3).

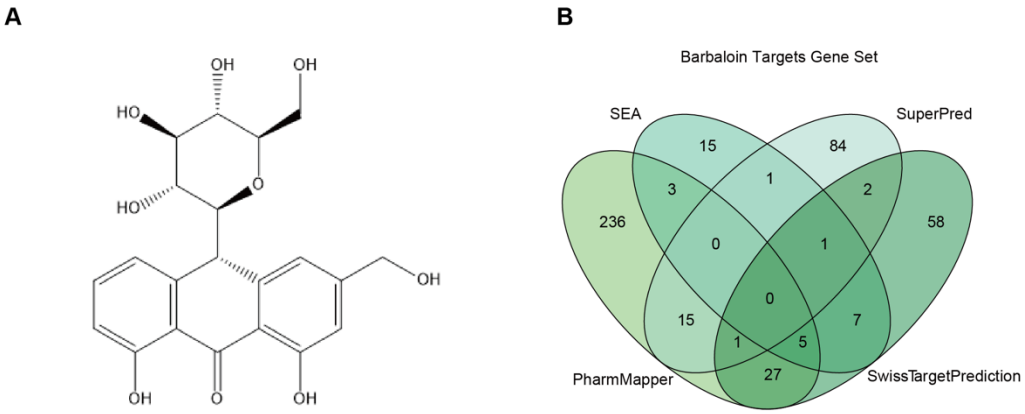

Figure 2. A) 2D structure of barbaloin and B) prediction of potential target genes through platforms of SEA, SuperPred, PharmMapper, and SwissTargetPrediction.

2.3. Identification and Functional Characterization of Key Target Genes Linking Barbaloin to Lung Transplantation

To identify potential targets of barbaloin in the context of lung transplantation pathology, we identified the common genes at the intersection of four key sets: the 362 DEGs, the 278 genes derived from WGCNA modules, the 4,100 known lung transplantation-related genes from GeneCards and OMIM and 455 predicted barbaloin target genes. This integrated screening yielded 8 key target genes: PNP, IL-6, BCL2A1, PADI4, CDA, SELE, MMP9, and MMP8 (Figure 3A). A regulatory network was constructed using Cytoscape (version 3.9.0) to visualize the interactions between barbaloin and lung transplantation phenotype through these key target genes (Figure 3B), these genes show significantly upregulated at 1-2 hours post-reperfusion compared to the cit group ($p < 0.001$, Figure 3C). The diagnostic potential of these genes was evaluated using ROC curve analysis (Figure 3D). IL-6 and PNP both demonstrated high diagnostic accuracy for reperfusion injury, with area under the curve (AUC) values exceeding 0.85 (IL-6: AUC = 0.874, 95% CI: 0.827-0.922; PNP: AUC = 0.867, 95% CI: 0.820-0.914). Moreover, protein-protein interaction (PPI) network also shows that the IL-6 and PNP are the core nodes (score ≥ 0.4) (Figure 3E).

 doi:10.20944/preprints202604.0528.v1

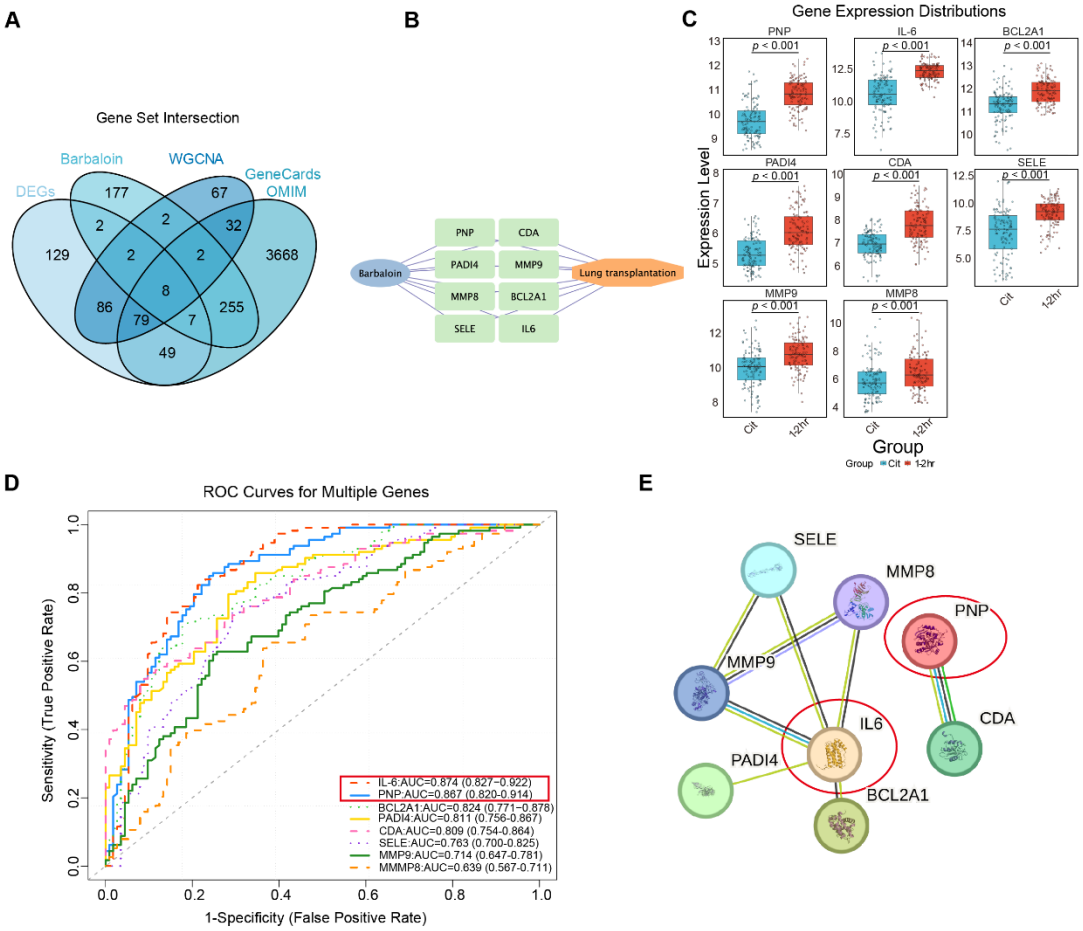

Figure 3. Identification and functional analysis of barbaloin-related target genes in lung transplantation. A) Venn diagram showing the intersection of gene sets: barbaloin target genes, WGCNA-derived module genes, lung transplantation-related genes (from GeneCards and OMIM) and DEGs. B) Regulatory network of barbaloin-key target genes-lung transplantation. C) Boxplots verifying the expression of key target genes in the merged transcriptomic dataset. D) ROC curves evaluating the diagnostic performance of key target genes. E) Protein-protein interaction (PPI) network of key target genes.

2.4. Immunological Characterization and Pathway Functional Annotation of Core Hub Genes

To elucidate the immunological functions of the core hub genes IL-6 and PNP during early post-reperfusion injury, we performed single-sample gene set enrichment analysis (ssGSEA) followed by correlation analysis. ssGSEA revealed profound remodeling of the immune microenvironment after reperfusion, with significant changes in the infiltration levels of 21 out of 28 immune cell subsets compared to the cit group (Figure 4A，B). Notably, the $CD4^+$ T-cell compartment was broadly and strongly activated ($p < 0.001$), including both pro-inflammatory (Th1, Th17) and regulatory (Treg) subsets, reflecting disrupted immune homeostasis alongside active counter-regulation. Spearman correlation analysis revealed that both two core hub genes are positively correlated with the activation of key innate and adaptive immune cells, including neutrophils, Th1 cells, and dendritic cells (Figure 4C). Furthermore, IL-6 and PNP were significantly enriched in major pro-inflammatory cascades, such as IL-17, TNF and NF-κB signaling, establishing them as central drivers of the dysregulated immune response and inflammatory amplification in early lung allograft injury (Figure 4D, E).

 doi:10.20944/preprints202604.0528.v1

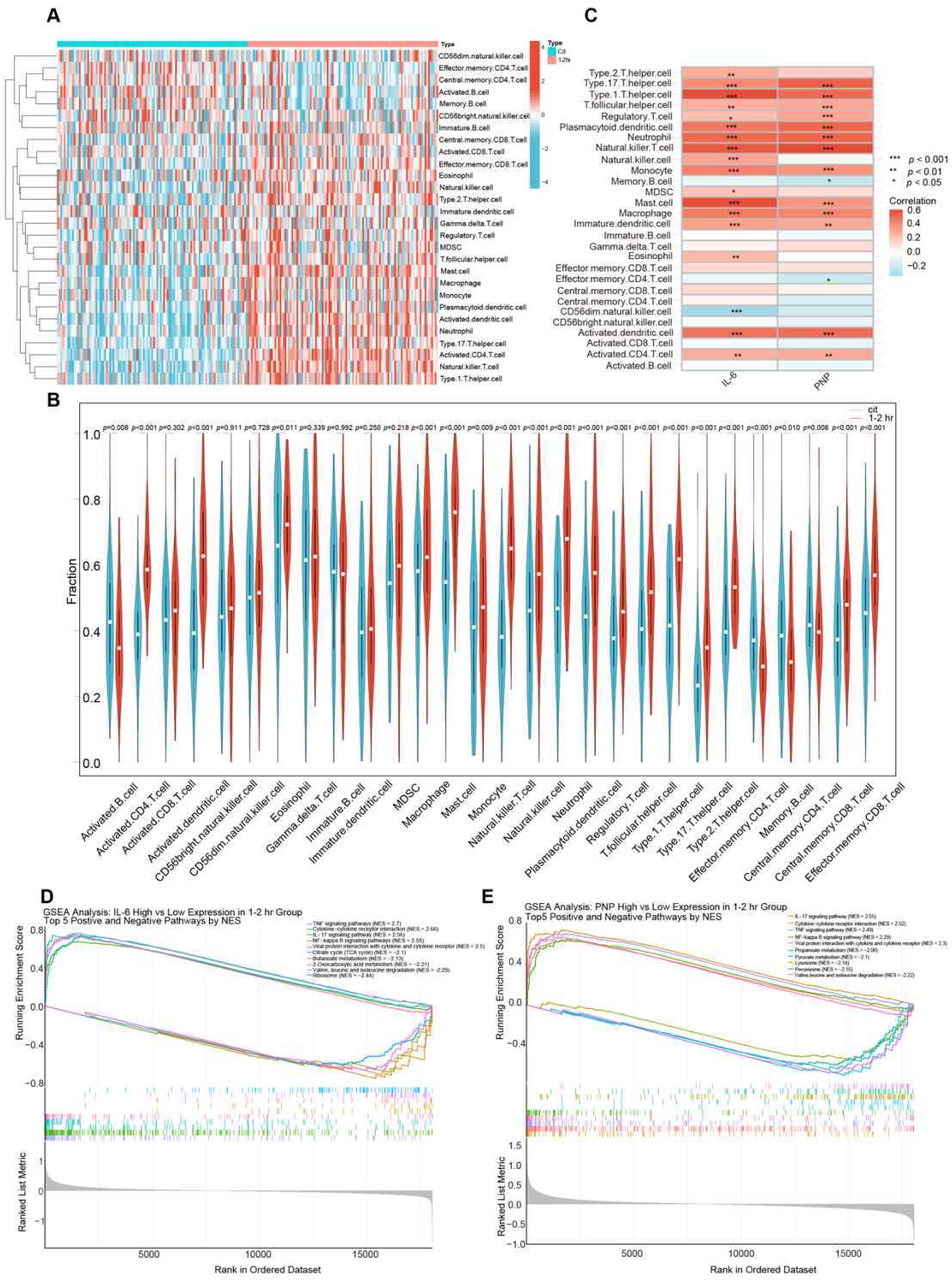

Figure 4. Single-sample gene set enrichment analysis (ssGSEA) and Gene Set Enrichment Analysis (GSEA) analyses of hub genes. A) Heatmap of ssGSEA scores for 28 immune cell types, grouped by condition (cit vs. 1-2 hr). B) Violin plots comparing immune cell enrichment scores between cit and 1-2hr groups, with Wilcoxon p-values shown. C) Spearman correlation heatmap between the expression of hub genes (IL-6, PNP) and immune cell enrichment scores within the 1-2hr group. *$p < 0.05$, **$p < 0.01$, ***$p < 0.001$. D-E) GSEA results for IL-6 and PNP.

2.5. Cellular Mapping of Core Hub Genes by Single-Cell Transcriptomics

To precisely map the cellular expression dynamics of the core hub genes IL-6 and PNP during early graft injury, we analyzed longitudinal single-cell RNA-seq data from six lung transplant

 doi:10.20944/preprints202604.0528.v1

recipients (GSE220797), encompassing matched samples from cold preservation (cit) and 2-hour reperfusion time points (2 hr) (Supplementary Figure S3 details the quality control). Unsupervised clustering of 104, 127 high-quality cells defined 14 distinct cell populations, which were rigorously annotated using canonical lineage-specific markers (Figure 5A， B). Analysis revealed highly distinct and complementary cellular expression patterns for the two core hub genes following reperfusion (Figure 5C-F). IL-6 expression was highly inducible and cell type-specific, with marked upregulation in endothelial and myeloid cells after reperfusion (Figure 5C， D). Conversely, PNP exhibited broad, constitutive expression across diverse structural and immune cell types, with a more moderate but widespread upregulation post-reperfusion (Figure 5E, F). Collectively, these single-cell resolution results prompt that IL-6 and PNP coordinately contribute to the early cellular response to reperfusion injury.

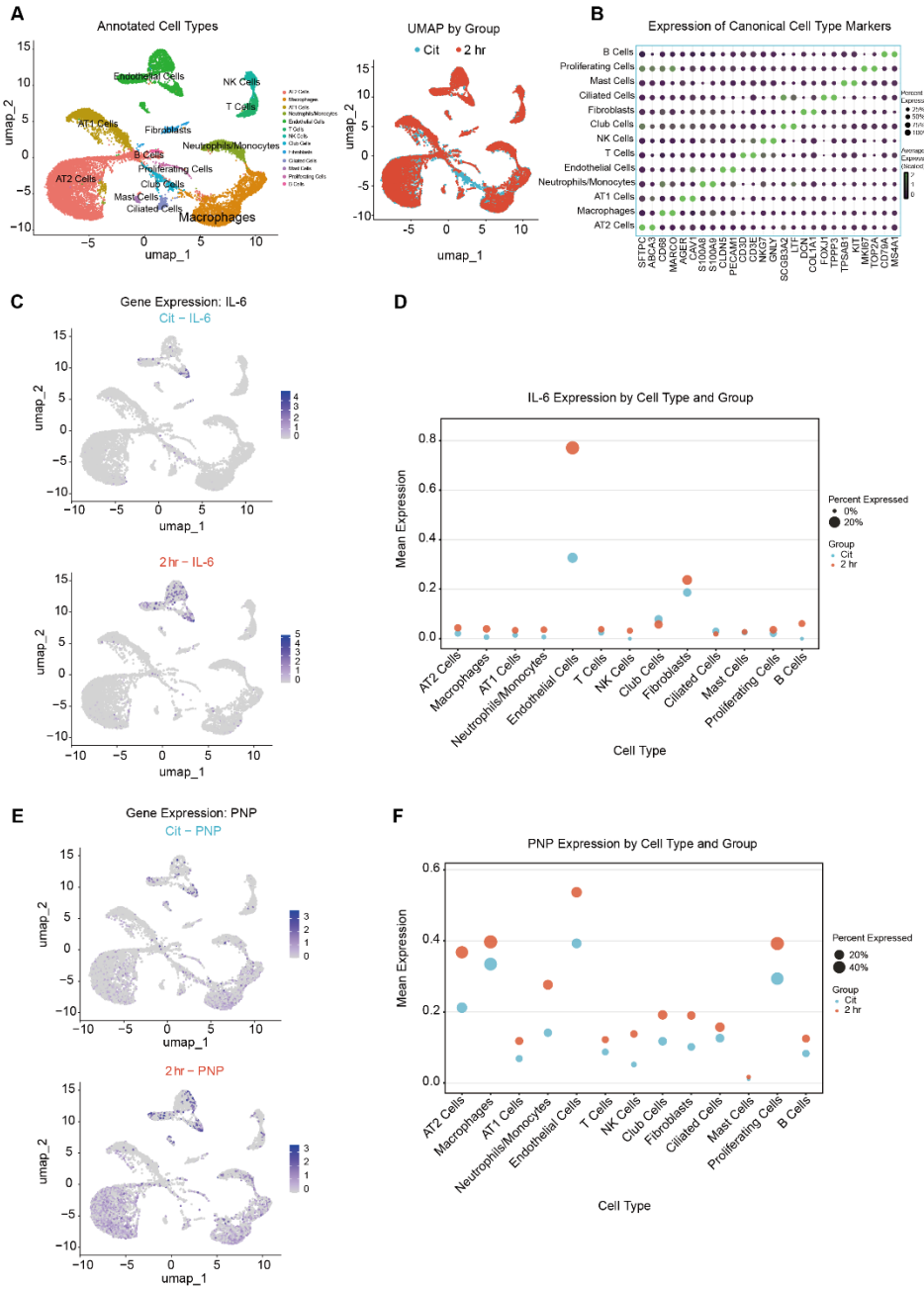

Figure 5. Single-cell transcriptomic landscape of lung transplantation samples. A) Uniform Manifold Approximation and Projection (UMAP) visualization of 104, 127 cells from 12 lung transplant samples, colored

 doi:10.20944/preprints202604.0528.v1

by annotated cell type (left) and by experimental condition (right: cit vs. 2 hr). B) Dot plot validating cell type annotation through the expression of canonical lineage-specific markers. C, E) UMAP plots illustrating IL-6 (C) and PNP (E) expression in cit (top) and 2 hr (bottom) groups. D, F) Dot plots showing IL-6 (D) and PNP (F) expression levels across cell types, stratified by experimental group.

2.6. Molecular Docking and Molecular Dynamics Simulations of Barbaloin with Core Hub Targets

To elucidate the potential interactions between barbaloin and the identified core hub genes, we employed molecular docking (MD) and molecular dynamics simulations (MDS) for both IL-6 and PNP. The result in Figure 6A and Figure 6B show that Barbaloin formed a complex with IL-6 at a calculated binding affinity of -7.6 kcal/mol. The ligand was positioned within a functional domain of IL-6, engaging key interfacial residues including LYS66, MET67, PHE74, SER169, GLU172, PHE173, GLN175, SER176, and ARG179 (Figure 6C). Especially, SER169, GLU172, PHE173, GLN175 residues within the critical region spanning residues 128-175 of human IL-6, which has been experimentally demonstrated to be essential for IL-6 biological activity, highlighting the functional relevance of this interaction site for potential modulation of IL-6 signaling [10]. For PNP, the docking affinity was slightly stronger at -8.3 kcal/mol (Figure 6G, H). Barbaloin localized to the active site of PNP, with interactions involving residues PHE200, GLU201, THR202, VAL203, ASN243, LYS244, VAL245, ILE246, GLU250, SER251, GLU253, LYS254, ALA255, ASN256, and HIS257 (Figure 6I). Notably, PHE200, GLU201, and ASN243 are critical residues constituting the catalytic and substrate-binding pocket of human PNP [11]. This suggests barbaloin may directly interfere with the enzymatic function of PNP through competitive or allosteric mechanisms. Figure D-F, J-L show the structural compactness and stability of both bound complexes. In summary, the integrated computational analyses demonstrate that barbaloin can form stable, energetically favorable complexes with both IL-6 and PNP, providing a structural rationale for its potential to modulate these key targets in the context of lung transplant injury.

 doi:10.20944/preprints202604.0528.v1

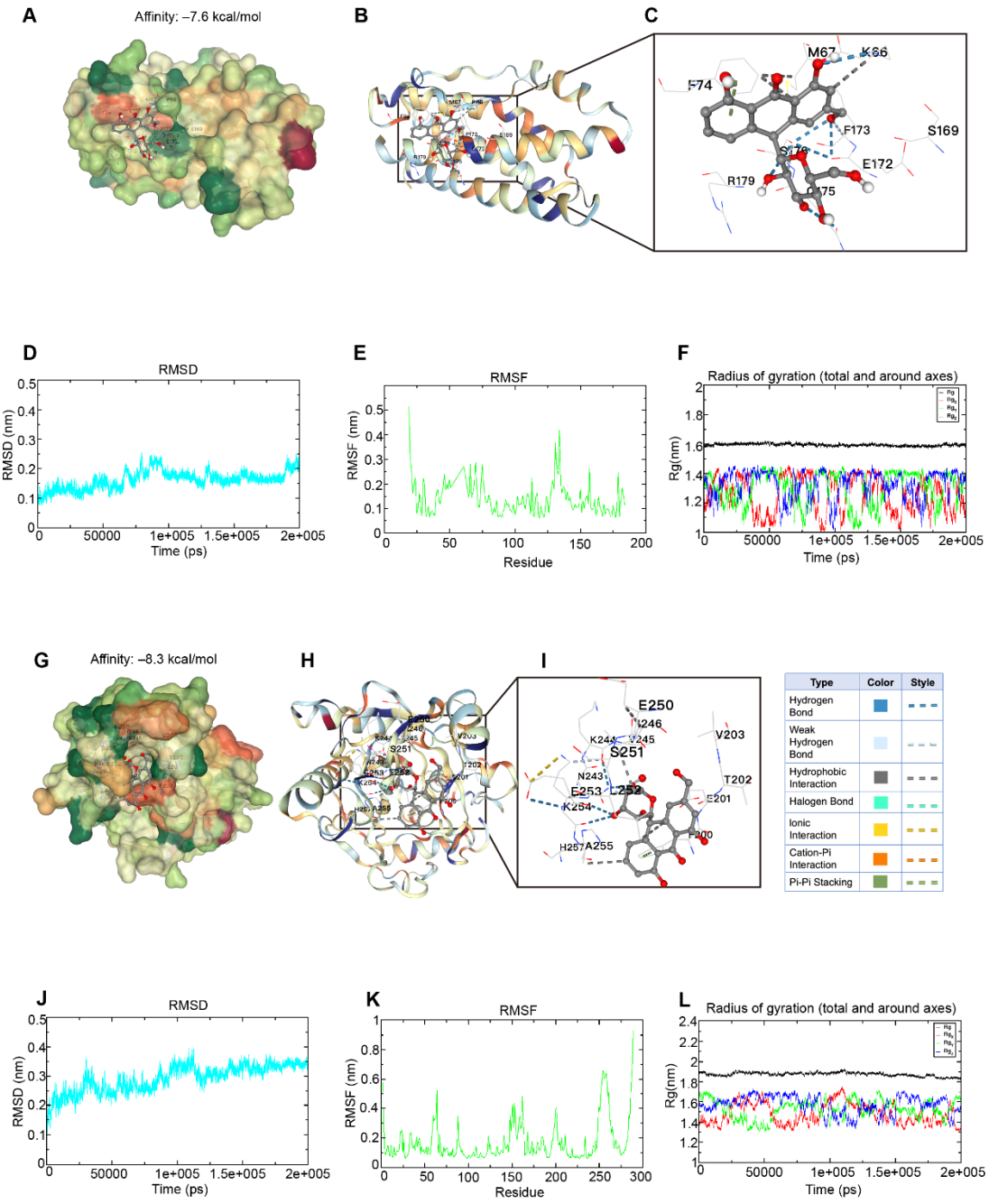

Figure 6. Molecular docking and MD simulations of barbaloin with IL-6 and PNP. A-C) Barbaloin binds to IL-6 with an affinity of -7.6 kcal/mol. D-F) MD simulation analysis of the IL-6-barbaloin complex. (D) Backbone RMSD, (E) per-residue RMSF of IL-6, and (F) Rg of the complex. G-I) Barbaloin binds to PNP with an affinity of -8.3 kcal/mol. J-L) MD simulation analysis of the PNP-barbaloin complex. (J) Backbone RMSD, (K) per-residue RMSF of PNP, and (L) Rg of the complex.

2.7. QRT-PCR Analysis of Core Hub Genes in the In Vivo I/R Model

To validate the involvement of the core hub targets IL-6 and PNP in LIRI injury, we established a left LIRI model in C57BL/6J mice (Figure 7A). qRT-PCR analysis demonstrated that compared to the sham group, the mRNA expression levels of *il-6* (Figure 7B, $p < 0.001$) and *pnp* (Figure 7C, $p < 0.001$) in lung tissues were significantly upregulated in the I/R group. These findings confirm the participation of IL-6 and PNP in LIRI and align with the predicted expression trends from the preceding bioinformatic analysis.

 doi:10.20944/preprints202604.0528.v1

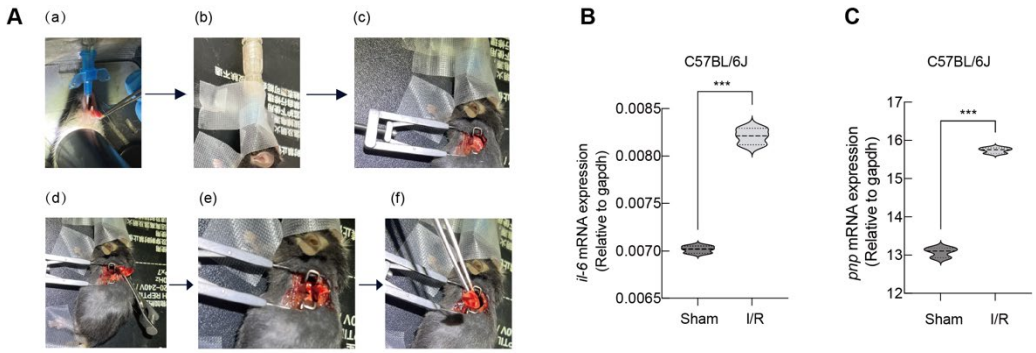

Figure 7. Left lung ischemia-reperfusion (I/R) injury model in C57BL/6J mice. A) Surgical workflow: (a) tracheal intubation, (b) mechanical ventilation, (c) thoracotomy and hilar exposure, (d) 15-min hilar clamping, (e) hilar release and reperfusion, (f) lung harvest after 20-min reperfusion. B-C) *Il-6* and *pnp* mRNA levels were significantly elevated in I/R vs. Sham. (Data are expressed as mean ± SD; B, C: unpaired two-tailed Student's t-test; ***$p < 0.001$ vs Sham group).

2.8. The Protective Mechanism of Barbaloin in the OGD/R Cell Model

To further investigate the mechanism of barbaloin's action, we established an in vitro model of IRI using OGD/R injury in human bronchial epithelial cells (BEAS-2B, ATCC CRL-9609). CCK-8 assays first confirmed that barbaloin had no significant cytotoxicity on BEAS-2B cells within the concentration range of 0-100 μM (Figure 8A). The OGD/R model induced a significant reduction in cell viability. However, this loss was reversed by barbaloin pre-treatment; significant recovery was observed at concentrations of 25, 50, and 75 μM ($p < 0.001$; Figure 8B). At the molecular level, qRT-PCR results showed that OGD/R injury significantly upregulated the mRNA expression of *IL-6* and *PNP* (Figure 8C, D), and barbaloin effectively reversed this upregulation. PNP enzyme activity assay further confirmed that barbaloin significantly inhibited the OGD/R -induced increase in PNP activity (Figure 8E). This indicates that barbaloin acts on the predicted targets IL-6 and PNP in vitro.

Further mechanistic studies revealed that the protective effect of barbaloin involves antioxidant and anti-inflammatory pathways. Firstly, barbaloin dose-dependently inhibited the OGD/R-induced excessive accumulation of ROS (Figure 8F, G). Secondly, immunofluorescence and Western blot analyses revealed that OGD/R stimulation induced significant nuclear translocation and phosphorylation of NF-κB p65, both of which were effectively suppressed by barbaloin pre-treatment (Figure 8 H-J). Concurrently, barbaloin significantly downregulated the OGD/R-induced protein expression levels of key NLRP3 inflammasome components, including NLRP3, the activated form of caspase-1 (cleaved caspase-1), and its downstream inflammatory cytokine IL-1β (Figure 8I, K-M).

 doi:10.20944/preprints202604.0528.v1

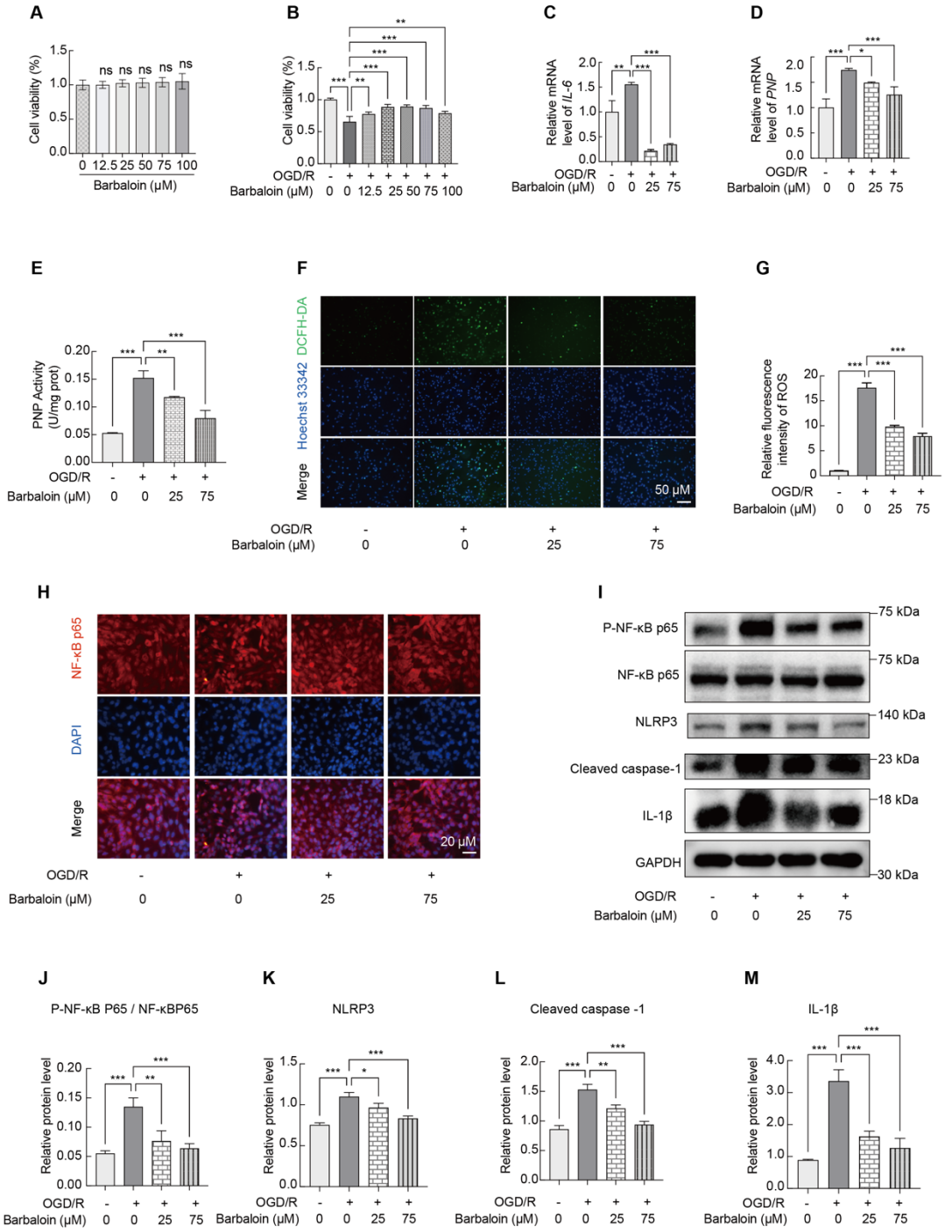

Figure 8. Barbaloin protects BEAS-2B cells against OGD/R injury by mitigating oxidative stress and inhibiting the NF-κB/NLRP3 pathway. A) CCK-8 assay of BEAS-2B cell viability after 24 h treatment with barbaloin (0-100 μM) under normal conditions. B) CCK-8 assay of BEAS-2B cell viability in the OGD/R model with barbaloin treatment. C, D) qRT-PCR analysis of *IL-6* (C) and *PNP* (D) mRNA expression in OGD/R-exposed BEAS-2B cells with or without barbaloin. E) PNP activity assay in OGD/R-exposed BEAS-2B cells with or without barbaloin. F) Intracellular ROS levels. G) Quantitative analysis the fluorescence intensity in each group. H) Immunofluorescence staining of NF-κB p65 (red) and DAPI (blue). I-M) Western blot analysis of P-NF-κB p65, NF-κB p65, NLRP3, Cleaved caspase-1and IL-1β protein expression (Data are mean ± SD. B: unpaired two-tailed Student's t-test; all other panels: one-way ANOVA with Tukey's test. *$p < 0.05$, **$p < 0.01$, ***$p < 0.001$; ns = not significant.).

 doi:10.20944/preprints202604.0528.v1

2.9. ADMET and Drug-Likeness Profiling of Barbaloin

ADMET (Absorption, Distribution, Metabolism, Excretion, Toxicity) profiling (Tables 1-3) characterized barbaloin as a Lipinski-compliant compound with high intestinal absorption (96.3%) and low risk of CYP450 interactions. While high plasma protein binding (93.54%) and a short half-life (0.635 h) were noted, its drug-likeness was supported by favorable SA and MCE-18 scores. Predicted risks for drug-induced liver injury (DILI) and mutagenicity highlight the need for targeted preclinical optimization to improve both safety and pharmacokinetic stability.

Table 1. Prediction of Toxicity Parameters of Barbaloin.

Propetry	Parameter	values	Unit
Absorption	Caco-2 Permeability	-5.892	(Log Papp)
	MDCK Permeability	4×10^{-6}	cm/s
	P-glycoprotein inhibitor	NO	categorical
	P-glycoprotein substrate	NO	categorical
	Human Intestinal Absorption	96.3	(% Absorbed)
Distribution	Volume Distribution	0.902	(L/kg)
	Plasma Protein Binding	93.54	(%)
	Blood-Brain Barrier Penetration	NO	categorical
	The fraction unbound in plasms	4.162	(%)
Metabolism	CYP1A2 inhibitor	NO	categorical
	CYP1A2 substrate	NO	categorical
	CYP2C19 inhibitor	NO	categorical
	CYP2C19 substrate	NO	categorical
	CYP2C9 inhibitor	NO	categorical
	CYP2C9 substrate	NO	categorical
	CYP2D6 inhibitor	NO	categorical
	CYP2D6 substrate	NO	categorical
	CYP3A4 inhibitor	NO	categorical
	CYP3A4 substrate	NO	categorical
Excretion	Clearance	6.166	(mL/min/kg)
	Half-life	0.635	(hour)
Toxicity	hERG Blockers	NO	categorical
	hERG Blockers (10um)	NO	categorical
	Drug Induced Liver Injuy	Yes	categorical
	AMES Toxicity	Yes	categorical
	Rat Oral Acute Toxicity	NO	categorical
	FDA Maximum (Recommended) Daily Dose	NO	categorical
	Skin Sensitization	Yes	categorical
	Respiratory Toxicity	NO	categorical

Table 2. Physicochemical Properties of Barbaloin.

Compounds	Formula	Mol weight	Volume	nHA	nHD	nRot	nRing	nHet	fChar	nRig	TPSA
Barbaloin	$C_{21}H_{22}O_9$	418.13	398.203	9	7	3	4	9	0	23	167.91

Note. The general recommended ranges are as follows: a) Molecular weight, 100 to 600. b) nHA-Number of H bond acceptors, <12. c) nHD-Number of rotatable bonds, <7. d) nRot-Number of rotatable bonds, <11. e) nRing-Number of rings, <6. f) nHet-Number of heteroatoms,1to15. g) fChar-Formal charge,-4 to 4. h) nRig-Number of rigid bonds, <30. I) TPSA-Topological Polar Surface Area,<140.

Table 3. Drug-likeliness Properties of Barbaloin.

 doi:10.20944/preprints202604.0528.v1

Compounds	logP	logS	Lipinski Rule	Pfizer Rule	GSK Rule	Golden Triangle	PAINS	SAscore	MCE-18	Fsp3	GASA
Barbaloin	0.623	-1.916	Accepted	Accepted	Rejected	Accepted	0	4.173	88.759	0.381	1

Note. logP-Lipophilicity, logS-Water solubility, SAscore-Synthetic accessibility score, Fsp3-sp3 hybridized carbons.

3. Discussion

This study provides a comprehensive, multi-faceted investigation into the molecular pathogenesis of early LIRI and identifies the natural compound barbaloin as a promising therapeutic candidate. By integrating bulk and single-cell transcriptomics, network pharmacology, computational biology, and mechanistic in vitro experiments, we delineate a coherent pathway from disease phenotype characterization to drug-target validation.

Our initial transcriptomic analysis established the foundational phenotype of early LIRI: a concurrent hyperactivation of pro-inflammatory pathways (e.g., IL-17, TNF, NF-κB) and a broad suppression of core metabolic processes. This dichotomy highlights the profound bioenergetic cost of the acute inflammatory response post-reperfusion [12,13]. The subsequent integrative screening, converging differentially expressed genes, phenotype-associated co-expression modules, known lung transplantation genes, and predicted barbaloin targets, robustly pinpointed eight key genes. Among these, IL-6 and PNP emerged as core hubs based on their central positions in protein interaction networks and superior diagnostic performance for reperfusion injury. This finding is significant as it bridges a classic, potent cytokine (IL-6) with a key enzyme in purine salvage metabolism (PNP), suggesting an intertwined mechanism linking inflammatory signaling and metabolic reprogramming in graft injury [14,15].

The functional and immunological profiling of IL-6 and PNP revealed a nuanced, collaborative role. While both genes co-activated a central inflammatory axis, their correlation patterns with immune cell subsets and single-cell expression localization indicated functional collaboration. IL-6, primarily induced in endothelial cells and myeloid lineages, appears to function as a master regulator of the inflammatory milieu, balancing pro-inflammatory and regulatory signals [16,17]. In contrast, PNP, constitutively expressed across diverse cell types and further upregulated post-reperfusion, likely supports the heightened metabolic demand and fine-tunes specific effector immune responses, particularly those involving Th17 cells and pDCs. This dual-target paradigm suggests that a therapeutic strategy simultaneously modulating both inflammatory signaling and purinergic metabolism may be more effective than targeting either axis alone [18].

The computational studies provided a robust structural rationale for barbaloin's interaction with both IL-6 and PNP. The stable binding poses and favorable dynamics simulations suggest these are not merely theoretical targets but are plausibly engaged by the compound. In vivo validation confirmed the significant upregulation of IL-6 and PNP in LIRI mouse models. Mechanistically, barbaloin protected bronchial epithelial cells from OGD/R injury by modulating the IL-6/PNP axis. By curbing IL-6-mediated inflammatory signaling and PNP-driven purine catabolism, barbaloin effectively attenuated ROS production [19–21]. This reduction in oxidative stress subsequently inhibited the NF-κB/NLRP3 inflammasome pathway, thereby preserving cellular integrity [22].

The favorable ADMET and drug-likeness profile of barbaloin, particularly its high intestinal absorption and low CYP450 interaction potential, supports its feasibility for further development. However, the predicted alerts for hepatotoxicity (DILI) and mutagenicity necessitate careful preclinical toxicological evaluation. Strategies such as structural modification or formulation development could be explored to mitigate these risks while preserving efficacy [23,24].

4. Materials and Methods

4.1. Integrated Bulk Transcriptomic Analysis

 doi:10.20944/preprints202604.0528.v1

This study integrated transcriptomic data from two independent datasets on human lung transplantation (GSE127004 with 46 sample pairs and GSE145989 with 67 sample pairs) [25,26]. All samples were derived from peripheral lung biopsies, collected both at the end of cold ischemia and after 1-2 hours of reperfusion, forming a total of 113 matched pairs. After merging the datasets, batch effect correction and normalization were applied.

4.2. Identification of Differentially Expressed Genes (DEGs) in Lung Transplantation

To DEGs between cold ischemia and early reperfusion (1-2 hours post-reperfusion) in lung transplantation, we performed an integrated analysis of the merged transcriptomic dataset. Using the "limma" package (version 3.62.2), DEGs were screened using the thresholds of $|\log_2 FC| \geq 0.585$ and an $q < 0.05$.

4.3. Weighted Gene Co-Expression Network Analysis (WGCNA)

A weighted gene co-expression network was constructed using the "WGCNA" package (version 1.73). The soft-thresholding power was optimized to attain scale-free topology, and co-expression modules were identified through hierarchical clustering with dynamic tree cutting. Modules significantly correlated with lung transplantation status (based on module-trait relationships) were selected for further validation. Within these key modules, we assessed biological coherence by evaluating the correlation between gene significance (GS, the absolute correlation of gene expression with the phenotype) and module membership (MM, the correlation of gene expression with the module eigengene). A strong GS-MM correlation indicates functional unity of the module. Genes from all phenotypes-associated modules were merged to form a candidate gene set for downstream analysis.

4.4. Retrieval of Lung Transplantation-Related Genes from Public Databases

Lung transplantation-related genes were retrieved by querying the GeneCards (https://www.genecards.org/) [27]and OMIM databases (https://www.omim.org/) [28] using the keyword "Lung transplantation", where results from GeneCards were filtered with a relevance score threshold of ≥ 5, followed by taking the union of the identified gene sets from both sources to generate a comprehensive reference list.

4.5. Collection of Barbaloin Targets

To identify the putative targets of Barbaloin, its canonical molecular structure information in both SMILES and SDF formats was obtained from the PubChem database (https://pubchem.ncbi.nlm.nih.gov/) [29]. This structural data was subsequently submitted as input to four independent target prediction platforms: PharmMapper (https://www.lilab-ecust.cn/pharmmapper/) [30], the Similarity Ensemble Approach (SEA, https://sea.bkslab.org/) [31], SuperPred (https://prediction.charite.de/) [32], and SwissTargetPrediction (http://swisstargetprediction.ch/) [33]. The predicted target genes from all four databases were standardized using UniProt, merged, and compiled into a comprehensive list of Barbaloin's potential targets [34].

4.6. Four-Set Intersection Analysis for Screening Key Target Genes

To identify high-confidence targets of Barbaloin in lung transplantation, a four-way intersection was performed among: (1) cold ischemia/reperfusion DEGs, (2) WGCNA-derived modules, (3) database-retrieved lung transplantation-related genes, and (4) putative Barbaloin targets. The overlapping genes, visualized via a Venn diagram, were designated as candidate key targets for further analysis. Subsequently, a barbaloin-target-lung transplantation regulatory network was constructed using Cytoscape (https://web.cytoscape.org) [35].

 doi:10.20944/preprints202604.0528.v1

4.7. Characterization of Key Targets: Expression, Diagnostic Evaluation, and PPI network

The key target genes were validated through multiple approaches. Differential expression in lung transplantation was visualized with boxplots ("ggplot2" package, version 3.5.2). The diagnostic potential of each gene was evaluated by generating Receiver Operating Characteristic (ROC) curves and calculating AUC values. Finally, PPI network was constructed via the STRING database (https://cn.string-db.org) using the key target genes as seeds [36].

4.8. Integrative Screening for Core Hub Genes

Core hub genes were identified using an integrated two-step screening strategy. Candidates were selected if they: 1) acted as core nodes in the PPI network, and 2) ranked among the top two genes with diagnostic AUC > 0.85 in ROC analysis. Two key genes were identified for further study.

4.9. ssGSEA and GSEA Analyses of Core Hub Genes

To characterize the immunological associations of the core hub genes, we performed ssGSEA using the immune.gmt gene set (MSigDB) to quantify enrichment scores for 28 immune cell types in the merged transcriptomic dataset. A Spearman correlation heatmap was generated to visualize associations between core hub gene expression and immune cell scores in the 1-2 h group. Additionally, GSEA was conducted for each core hub gene using the immunesigdb.gmt gene set (MSigDB) to identify linked immune-related pathways [37].

4.10. Single-Cell Sequencing Analysis

Single-cell RNA sequencing (scRNA-seq) was performed on lung biopsies from six lung transplant recipients collected after cold preservation and 2-hour reperfusion (GSE220797) [13]. Data were processed using the "Seurat" package (version 5.2.1). Quality filtering retained genes detected in ≥3 cells and cells expressing 200-6,000 genes with <20% mitochondrial reads. Data were normalized, and the top 2,000 variable genes were selected for downstream analysis. Dimensional reduction (PCA), graph-based clustering (resolution=0.5), and cell-type annotation using established marker genes were subsequently performed [38].

4.11. Molecular Docking

Molecular docking was performed to validate the interaction of barbaloin with its core hub genes. Barbaloin (PubChem CID: 12305761) was energy-minimized via the MM2 force field in ChemBio3D (version14.0) and converted to mol2 format. Crystal structures of PNP (PDB: 1M73) and IL-6 (PDB: 1ALU) were retrieved from the RCSB Protein Data Bank (https://www.rcsb.org). Docking simulations were carried out using CB-Dock2 (https://cadd.labshare.cn/cb-dock2/index.php) [39,40], which predicts binding cavities and calculates binding affinities; the conformation with the lowest binding affinity for each target was selected for visualization and analysis.

4.12. Molecular Dynamics Simulation

A 200 ns molecular dynamics simulation was performed using GROMACS 2023.2 with the CHARMM36 force field to assess the stability of the PNP-barbaloin and IL-6-barbaloin complexes. The systems were prepared using the CHARMM-GUI server [41], solvated in a TIP3P water box, neutralized, and equilibrated under NVT and NPT ensembles. Production runs were conducted with a 2 fs time step under NPT conditions. Trajectory analyses, including root-mean-square deviation (RMSD), root-mean-square fluctuation (RMSF), and radius of gyration (Rg), were performed to confirm the stable binding and structural integrity of both complexes throughout the simulation [42,43].

4.13. Lung Ischemia-Reperfusion Mouse Model

 doi:10.20944/preprints202604.0528.v1

LIRI was induced in 6-week-old C57BL/6J mice by hilar clamping. All animal procedures were approved by the Biomedical Ethics Committee of Health Science Center of Xi'an Jiaotong University (Approval No. XJTUAE2024-792) and were conducted in accordance with the National Institutes of Health Guide for the Care and Use of Laboratory Animals.

After tracheal intubation and mechanical ventilation, a left thoracotomy was performed to expose the lung hilum. Ischemia was achieved by clamping the hilum for 15 min using a non-traumatic microvascular clamp, followed by clamp removal for 20 min of reperfusion. Left lung tissues were then harvested for subsequent analysis [44].

4.14. Cell Culture and Hypoxia/Reoxygenation Model

Human bronchial epithelial cells (BEAS-2B, ATCC CRL 9609) were cultured in DMEM (11965092, Gibco) supplemented with 10% fetal bovine serum (FBS, 10099141, Gibco) at 37 °C in a normoxic incubator (21% O_2, 5% CO_2, 94% relative humidity). To simulate LIRI in vitro, an OGD/R model was established: cells were subjected to 12 h of hypoxia (1% O_2, 5% CO_2, balanced with N_2) in glucose-free DMEM containing barbaloin (0-100 μM, MedChemExpress, HY N0123), followed by 8 h of reoxygenation in complete DMEM (10% FBS) with corresponding barbaloin concentrations under normoxic conditions (21% O_2, 5% CO_2) [45].

4.15. In Vitro Functional and Molecular Assays

Cell viability and intracellular ROS levels were assessed using CCK-8 (C0037, Beyotime) and DCFH-DA staining (S1105S, Beyotime; 20 min, 37 °C), respectively, with fluorescence analyzed via ImageJ. PNP activity was determined using a commercial kit (BC6350, Solarbio). For molecular quantification, gene expression was analyzed by quantitative real-time polymerase chain reaction (qRT-PCR) using the $2^{-}\Delta\Delta Ct$ method with GAPDH as the internal control. Protein expression and localization were evaluated via western blot and immunofluorescence (IF) assays, with targets including key components of the NF-κB/NLRP3 pathway (P-NF-κB p65, NF-KB p65, NLRP3, IL-1β, and cleaved caspase-1). Expression levels were quantified using Quantity One Software (version 4.62) [46]. Detailed antibody information and primer sequences are provided in Supplementary Tables S4-5.

4.16. ADMET Property Prediction

To systematically evaluate the drug-likeness and safety profile of barbaloin, its ADMET (Absorption, Distribution, Metabolism, Excretion, and Toxicity) properties were predicted using the ADMETlab 2.0 online platform (https://admetmesh.scbdd.com/) [47]. The SMILES string of barbaloin was submitted to the tool, which calculated a comprehensive set of parameters based on its built-in predictive models. All predictions were performed using the tool's default settings.

4.17. Statistical Analysis

Data analysis was performed using R (version 4.4.0) and GraphPad Prism (version 9.0). Experimental data are expressed as mean ± standard deviation (SD) from three independent replicate experiments. For statistical comparisons, when data satisfied normality and homogeneity of variance assumptions, one-way analysis of variance (ANOVA) followed by Tukey's multiple comparisons test was used for comparisons among three or more groups, and unpaired two-tailed Student's t-test was applied for comparisons between two independent groups. Statistical significance was denoted as $*p < 0.05$, $**p < 0.01$, $***p < 0.001$; "ns" indicates not significant.

5. Conclusion

This work demonstrated that barbaloin serves as a promising therapeutic agent for LIRI by dual-targeting IL-6 and PNP, which effectively attenuates oxidative stress and suppresses the NF-κB/NLRP3 inflammasome pathway. Given its multi-target capacity to modulate both inflammatory

 doi:10.20944/preprints202604.0528.v1

and metabolic dysregulation, barbaloin offers a novel clinical strategy to complement current immunosuppressive regimens and improve graft outcomes in lung transplant recipients.

Supplementary Materials: The following supporting information can be downloaded at the website of this paper posted on Preprints.org.

Author Contributions: Huanhuan Dong: Methodology, Formal analysis, Data Curation, Writing - Original Draft Niuniu Dong: Methodology, Formal analysis, Validation Jinteng Feng: Supervision, Software, Funding acquisition Wenyu Peng: Conceptualization, Writing-Original Draft, Funding acquisition Zhiying Wang: Validation, Software, Yihan Lin: Validation Zixuan Zhao: Methodology, Xiaopeng Ma: Software, Rongxuan Jiang: Validation Yanpeng Zhang: Supervision Mao Sun: Formal analysis, Validation Guangjian Zhang: Project administration, Funding acquisition.

Funding: This research was funded by the National Natural Science Foundation of China, grant numbers 82470107 (awarded to Guangjian Zhang), 82302349 (awarded to Wenyu Peng) and 82400127 (awarded to Jinteng Feng). The APC was funded by the authors' affiliated institution.

Institutional Review Board Statement: The animal study protocol was approved by the Institutional Review Board (Biomedical Ethics Committee) of Health Science Center of Xi'an Jiaotong University (protocol code XJTUAE2024-792 and date of approval February 28, 2024).

Informed Consent Statement: Not applicable.

Data Availability Statement: All data generated or analyzed during this study are included in this article.

Conflicts of Interest: The authors declare there are no conflicts of interest/competing interests related to this work.

Abbreviations

The following abbreviations are used in this manuscript:

IRI	Ischemia-reperfusion injury
ROS	Reactive Oxygen Species
IL-6	Interleukin-6
PNP	Purine nucleoside phosphorylase
EC	Endothelial cell
PGD	Primary graft dysfunction
H/R	hypoxia/reoxygenation
GSEA	Gene Set Enrichment Analysis
DEGs	Differentially Expressed Genes
WGCNA	Weighted gene co-expression network
GS	Gene significance
MM	Module membership
2D	Two-dimensional
SEA	Similarity Ensemble Approach
AUC	Area under the curve
PPI	Protein-protein interaction
ssGSEA	Single-sample gene set enrichment analysis
MD	Molecular docking
MDS	Molecular dynamics simulations
BEAS-2B	Human bronchial epithelial cells
DILI	Drug-induced liver injury
CI	Confidence interval
CCK-8	Cell Counting Kit-8
ADMET	Absorption, Distribution, Metabolism, Excretion, Toxicity
ROC	Receiver operating characteristic
scRNA-seq	Single-cell RNA sequencing
RMSD	Root-mean-square deviation

 doi:10.20944/preprints202604.0528.v1

RMSF	Root-mean-square fluctuation
Rg	Radius of gyration
FBS	Fetal bovine serum
qRT-PCR	Quantitative real-time polymerase chain reaction
IF	Immunofluorescence
GAPDH	Glyceraldehyde-3-phosphate dehydrogenase

References

1. Talaie, T., L. DiChiacchio, N.K. Prasad, C. Pasrija, W. Julliard, D.J. Kaczorowski, Y. Zhao, and C.L. Lau, *Ischemia-reperfusion Injury in the Transplanted Lung: A Literature Review.* Transplant Direct, 2021. **7**(2): p. e652.
2. Laubach, V.E. and A.K. Sharma, *Mechanisms of lung ischemia-reperfusion injury.* Curr Opin Organ Transplant, 2016. **21**(3): p. 246-52.
3. Chen-Yoshikawa, T.F., Ischemia-Reperfusion Injury in Lung Transplantation. Cells, 2021. **10**(6).
4. Zhang, Y., J. Sun, Y. Lin, R. Jiang, N. Dong, H. Dong, P. Li, J. Feng, Z. Zhu, and G. Zhang, *Machine learning-based prediction model for lung ischemia-reperfusion injury: insights from disulfidptosis-related genes.* Front Pharmacol, 2025. **16**: p. 1545111.
5. Li, Q. and H. Nie, Advances in lung ischemia/reperfusion injury: unraveling the role of innate immunity. Inflamm Res, 2024. **73**(3): p. 393-405.
6. Patel, D.K., K. Patel, and V. Tahilyani, *Barbaloin: a concise report of its pharmacological and analytical aspects.* Asian Pac J Trop Biomed, 2012. **2**(10): p. 835-8.
7. Wang, Y., H. Wang, and F. Yang, Barbaloin Treatment Contributes to the Rebalance of Glucose and Lipid Homeostasis of Gestational Diabetes Mellitus Mice. Dose Response, 2020. **18**(4): p. 1559325820984910.
8. Jiang, K., S. Guo, C. Yang, J. Yang, Y. Chen, A. Shaukat, G. Zhao, H. Wu, and G. Deng, Barbaloin protects against lipopolysaccharide (LPS)-induced acute lung injury by inhibiting the ROS-mediated PI3K/AKT/NF-κB pathway. Int Immunopharmacol, 2018. **64**: p. 140-150.
9. Zhang, P., X. Liu, G. Huang, C. Bai, Z. Zhang, and H. Li, *Barbaloin pretreatment attenuates myocardial ischemia-reperfusion injury via activation of AMPK.* Biochem Biophys Res Commun, 2017. **490**(4): p. 1215-1220.
10. Liu, H., J. Duan, J. Wang, S. Peng, and M. Zou, *Residues K128-Q175 of human interleukin-6 are essential for its biological activity.* Biochem Mol Biol Int, 1997. **42**(5): p. 1045-50.
11. Khandazhinskaya, A., I. Fateev, B. Eletskaya, A. Maslova, I. Konstantinova, K. Seley-Radtke, S. Kochetkov, and E. Matyugina, *Design and Synthesis of New Modified Flexible Purine Bases as Potential Inhibitors of Human PNP.* Molecules, 2023. **28**(3).
12. McGaugh, S., T. Chakrala, R. Prakash, and K. Motaparthi, *Acute inflammatory edema in the setting of bilateral lung transplantation.* JAAD Case Rep, 2023. **32**: p. 32-34.
13. Wong, A., A. Duong, G. Wilson, J. Yeung, S. MacParland, H. Han, M. Cypel, S. Keshavjee, and M. Liu, *Ischemia-reperfusion responses in human lung transplants at the single-cell resolution.* Am J Transplant, 2024. **24**(12): p. 2199-2211.
14. Lu, P., R. Shen, J. Yang, L. Wu, and R. Wang, Dynamic regulation and targeted interventions of macrophages in ischemia-reperfusion injury. J Adv Res, 2026. **80**: p. 705-723.
15. Goda, Y., N.S. Sharma, A.S. Potter, and D. Hayes, Jr., Airway epithelial cell chimerism and chronic lung allograft dysfunction associated with ischemia-reperfusion-injury in lung transplantation. Curr Opin Organ Transplant, 2025. **30**(5): p. 365-371.
16. Pirlet, E., L. Alders, P.M. Pincela Lins, and A. Bronckaers, *Updated Mechanisms of IL-6 in Human Endothelial Cells.* Faseb j, 2025. **39**(17): p. e71001.
17. Wolf-Johnston, A., Y. Ikeda, I. Zabbarova, A.J. Kanai, S. Bastacky, R. Moldwin, J.N. Stern, E.K. Jackson, and L.A. Birder, *Purine nucleoside phosphorylase inhibition is an effective approach for the treatment of chemical hemorrhagic cystitis.* JCI Insight, 2024. **9**(5).
18. Jo, H.G., C.Y. Baek, S. Ilyas, Y. Hwang, E. Baek, H.S. Song, and D. Lee, Asarum heterotropoides F. schmidt attenuates osteoarthritis via multi-target anti-inflammatory actions: A network pharmacology and experimental validation. J Ethnopharmacol, 2025. **349**: p. 119915.

 doi:10.20944/preprints202604.0528.v1

19. Velusamy, P., D.J. Buckley, J.L. Greaney, A.J. Case, P.J. Fadel, and D.W. Trott, *IL-6 induces mitochondrial ROS production and blunts NO bioavailability in human aortic endothelial cells.* Am J Physiol Regul Integr Comp Physiol, 2025. **328**(4): p. R509-r514.
20. Yang, B., X. Yang, X. Sun, J. Shi, Y. Shen, and R. Chen, IL-6 Deficiency Attenuates Skeletal Muscle Atrophy by Inhibiting Mitochondrial ROS Production through the Upregulation of PGC-1α in Septic Mice. Oxid Med Cell Longev, 2022. **2022**: p. 9148246.
21. Birder, L.A. and E.K. Jackson, Dysregulated Purine Metabolism Contributes to Age-Associated Lower Urinary Tract Dysfunctions. Adv Geriatr Med Res, 2021. **3**(4).
22. He, Y., Z. Li, T. Xu, D. Luo, Q. Chi, Y. Zhang, and S. Li, Polystyrene nanoplastics deteriorate LPS-modulated duodenal permeability and inflammation in mice via ROS drived-NF-κB/NLRP3 pathway. Chemosphere, 2022. **307**(Pt 1): p. 135662.
23. Liu, Q., H. Sun, X. Li, H. Sheng, and L. Zhu, Strategies for Solubility and Bioavailability Enhancement and Toxicity Reduction of Norcantharidin. Molecules, 2022. **27**(22).
24. Sorour, A.A., R.G. Aly, H.M. Ragab, and A. Wahid, Structure Modification Converts the Hepatotoxic Tacrine into Novel Hepatoprotective Analogs. ACS Omega, 2024. **9**(2): p. 2491-2503.
25. Sessa, A., L. Fagnocchi, G. Mastrototaro, L. Massimino, M. Zaghi, M. Indrigo, S. Cattaneo, D. Martini, C. Gabellini, C. Pucci, A. Fasciani, R. Belli, S. Taverna, M. Andreazzoli, A. Zippo, and V. Broccoli, *SETD5 Regulates Chromatin Methylation State and Preserves Global Transcriptional Fidelity during Brain Development and Neuronal Wiring.* Neuron, 2019. **104**(2): p. 271-289.e13.
26. Baciu, C., J. Shin, M. Hsin, M. Cypel, S. Keshavjee, and M. Liu, *Altered purine metabolism at reperfusion affects clinical outcome in lung transplantation.* Thorax, 2023. **78**(3): p. 249-257.
27. Stelzer, G., N. Rosen, I. Plaschkes, S. Zimmerman, M. Twik, S. Fishilevich, T.I. Stein, R. Nudel, I. Lieder, Y. Mazor, S. Kaplan, D. Dahary, D. Warshawsky, Y. Guan-Golan, A. Kohn, N. Rappaport, M. Safran, and D. Lancet, *The GeneCards Suite: From Gene Data Mining to Disease Genome Sequence Analyses.* Curr Protoc Bioinformatics, 2016. **54**: p. 1.30.1-1.30.33.
28. Amberger, J.S., C.A. Bocchini, A.F. Scott, and A. Hamosh, *OMIM.org: leveraging knowledge across phenotype-gene relationships.* Nucleic Acids Res, 2019. **47**(D1): p. D1038-d1043.
29. Kim, S., J. Chen, T. Cheng, A. Gindulyte, J. He, S. He, Q. Li, B.A. Shoemaker, P.A. Thiessen, B. Yu, L. Zaslavsky, J. Zhang, and E.E. Bolton, *PubChem 2023 update.* Nucleic Acids Res, 2023. **51**(D1): p. D1373-d1380.
30. Wang, X., Y. Shen, S. Wang, S. Li, W. Zhang, X. Liu, L. Lai, J. Pei, and H. Li, PharmMapper 2017 update: a web server for potential drug target identification with a comprehensive target pharmacophore database. Nucleic Acids Res, 2017. **45**(W1): p. W356-w360.
31. Wang, Z., L. Liang, Z. Yin, and J. Lin, *Improving chemical similarity ensemble approach in target prediction.* J Cheminform, 2016. **8**: p. 20.
32. Nickel, J., B.O. Gohlke, J. Erehman, P. Banerjee, W.W. Rong, A. Goede, M. Dunkel, and R. Preissner, *SuperPred: update on drug classification and target prediction.* Nucleic Acids Res, 2014. **42**(Web Server issue): p. W26-31.
33. Daina, A., O. Michielin, and V. Zoete, SwissTargetPrediction: updated data and new features for efficient prediction of protein targets of small molecules. Nucleic Acids Res, 2019. **47**(W1): p. W357-w364.
34. UniProt: the Universal Protein Knowledgebase in 2023. Nucleic Acids Res, 2023. **51**(D1): p. D523–d531.
35. Ono, K., D. Fong, C. Gao, C. Churas, R. Pillich, J. Lenkiewicz, D. Pratt, A.R. Pico, K. Hanspers, Y. Xin, J. Morris, M. Kucera, M. Franz, C. Lopes, G. Bader, T. Ideker, and J. Chen, *Cytoscape Web: bringing network biology to the browser.* Nucleic Acids Res, 2025. **53**(W1): p. W203-w212.
36. Szklarczyk, D., A.L. Gable, D. Lyon, A. Junge, S. Wyder, J. Huerta-Cepas, M. Simonovic, N.T. Doncheva, J.H. Morris, P. Bork, L.J. Jensen, and C.V. Mering, *STRING v11: protein-protein association networks with increased coverage, supporting functional discovery in genome-wide experimental datasets.* Nucleic Acids Res, 2019. **47**(D1): p. D607-d613.
37. Subramanian, A., P. Tamayo, V.K. Mootha, S. Mukherjee, B.L. Ebert, M.A. Gillette, A. Paulovich, S.L. Pomeroy, T.R. Golub, E.S. Lander, and J.P. Mesirov, *Gene set enrichment analysis: a knowledge-based approach for interpreting genome-wide expression profiles.* Proc Natl Acad Sci U S A, 2005. **102**(43): p. 15545-50.

 doi:10.20944/preprints202604.0528.v1

38. Gao, J., X. Jiang, Z. Zhang, N. Zhang, Z. Xia, Y. Fu, Y. Jin, C. Chen, and Z. Wen, Integrative analysis of scRNA-seq and bulk RNA-seq to identify lactylation-related gene signatures in lung ischemia-reperfusion injury after lung transplantation. Int Immunopharmacol, 2025. **165**: p. 115361.
39. Liu, Y. and Y. Cao, *Protein-Ligand Blind Docking Using CB-Dock2*. Methods Mol Biol, 2024. **2714**: p. 113-125.
40. Liu, Y., X. Yang, J. Gan, S. Chen, Z.X. Xiao, and Y. Cao, CB-Dock2: improved protein-ligand blind docking by integrating cavity detection, docking and homologous template fitting. Nucleic Acids Res, 2022. **50**(W1): p. W159-w164.
41. Guterres, H. and W. Im, CHARMM-GUI-Based Induced Fit Docking Workflow to Generate Reliable Protein-Ligand Binding Modes. J Chem Inf Model, 2023. **63**(15): p. 4772-4779.
42. Terteci-Popescu, A.E. and T.A. Beu, Branched polyethyleneimine: CHARMM force field and molecular dynamics simulations. J Comput Chem, 2022. **43**(31): p. 2072-2083.
43. Wu, X., L.Y. Xu, E.M. Li, and G. Dong, *Application of molecular dynamics simulation in biomedicine.* Chem Biol Drug Des, 2022. **99**(5): p. 789-800.
44. Weng, G., Y. Chen, S. Bao, C. Zhang, and W. Gong, *A mouse model of lung ischemia-reperfusion injury with reversible left hilar entrapment.* Animal Model Exp Med, 2025. **8**(9): p. 1717-1724.
45. Ashraf, A., B. Zechmann, and E.D. Bruce, Hypoxia-inducible factor 1α modulates acrolein-induced cellular damage in bronchial epithelial cells. Toxicology, 2025. **515**: p. 154158.
46. Liu, X., R. Tang, J. Xu, Z. Tan, C. Liang, Q. Meng, Y. Lei, J. Hua, Y. Zhang, J. Liu, B. Zhang, W. Wang, X. Yu, and S. Shi, CRIP1 fosters MDSC trafficking and resets tumour microenvironment via facilitating NF-κB/p65 nuclear translocation in pancreatic ductal adenocarcinoma. Gut, 2023. **72**(12): p. 2329-2343.
47. Xiong, G., Z. Wu, J. Yi, L. Fu, Z. Yang, C. Hsieh, M. Yin, X. Zeng, C. Wu, A. Lu, X. Chen, T. Hou, and D. Cao, *ADMETlab 2.0: an integrated online platform for accurate and comprehensive predictions of ADMET properties.* Nucleic Acids Res, 2021. **49**(W1): p. W5-w14.